GEOPHYSICS®

Two-grid full-waveform Rayleigh-wave inversion via a genetic algorithm: part 1 – method and synthetic examples

Journal:	*Geophysics*
Manuscript ID	GEO-2018-0799.R2
Manuscript Type:	Technical Paper
Keywords:	surface wave, full-waveform inversion, near surface, shear wave (S-wave), dispersion
Area of Expertise:	Seismic Inversion, Engineering and Environmental Geophysics

Two-grid full-waveform Rayleigh-wave inversion via a genetic algorithm: part 1 – method and synthetic examples

Zhen Xing[1] and Alfredo Mazzotti[2]

Right Running Head: GA-FWI of Rayleigh waves – method

[1]Formerly University of Pisa, Department of Earth Sciences, Italy; presently CGG, Crawley, UK. E-mail: zhnxng@outlook.com.

[2]University of Pisa, Department of Earth Sciences, Italy. E-mail: alfredo.mazzotti@unipi.it.

ABSTRACT

When reliable a priori information is not available, it is difficult to correctly predict near-surface shear wave velocity models from Rayleigh waves through existing techniques, especially in the case of complex geology. To tackle this issue, we propose a new method, two-grid genetic-algorithm Rayleigh-wave full-waveform inversion (FWI). Adopting a two-grid parameterization of the model, the genetic algorithm inverts for unknown velocities and densities at the nodes of a coarse grid, while forward modeling is performed on a fine grid to avoid numerical dispersion. A bilinear interpolation brings the coarse-grid results into the fine-grid models. The coarse inversion grid allows for a significant reduction of the computing time required by the genetic algorithm to converge. The coarser the grid, the less the unknowns, the less the required computing time, at the expense of the model resolution. To further increase efficiency, our inversion code can perform the optimization employing an offset-marching strategy and/or a frequency-marching strategy, can make use of different kinds of objective

function and it allows for parallel computing. We illustrate the effect of the proposed inversion method using three synthetic examples with rather complex near-surface models. Though no a priori information was used in all the three tests, the long-wavelength structures of the reference models were fairly predicted, and satisfactory matches between “observed” and predicted data were achieved. The fair predictions of the reference models suggest that the final models estimated by our genetic-algorithm FWI, which we call macro-models, would be suitable input to gradient-based Rayleigh-wave FWI for further refinement. Other issues related to the practical use of the method are presented in a companion paper that shows the applications of the method to field data.

INTRODUCTION

Multichannel analysis of surface waves (MASW) (Park et al., 1999; Xia et al., 1999; Bohlen et al., 2004; Socco and Strobbia, 2004; Cercato, 2009; Maraschini et al., 2010; Socco et al., 2010, among others) is the current standard for Rayleigh-wave inversion, in which the observed data are given as the dispersion curves extracted from

frequency-wavenumber (f-k) or frequency-slowness (f-p) spectra. However, over the last few years, a new approach, full-waveform inversion (FWI) of Rayleigh waves, has emerged (Schäfer et al., 2013; Tran et al., 2013; Masoni et al, 2014; Groos et al, 2014; Masoni et al, 2016). This new approach seems to be promising because of several advantages over conventional techniques. First, instead of exploiting only the dispersion curves of the fundamental mode and of the higher modes, it makes use of the entire information (travel time, amplitude and phase) present in the recorded Rayleigh waves. Secondly, it naturally supports the predictions of multi-dimensional models. Thirdly, it requires no subjective interpretation, such as the picking of dispersion curves on f-p spectra of the observed data.

Nevertheless, the application of FWI to Rayleigh-wave field data is still rare. Schäfer et al. (2013) inverted Rayleigh-wave data to study a vertical fault system near Frankfurt, Germany, but they limited the inverted data within 10 Hz because adding higher frequencies would lead to local minima. Tran et al. (2013) used an FWI approach for sinkhole detection in Florida, United States. Groos et al. (2017) obtained reasonable

results by applying FWI to a Rayleigh-wave data set acquired at a gliding airfield near Karlsruhe, Germany.

However, due to the strong non-linearity of Rayleigh waves (Forbriger, 2003a, b; Rix, 2004; Brossier et al., 2009; Schäfer et al., 2013), local optimization methods, which require the computation of the gradient of the objective function, need adequate initial models to avoid getting trapped into local minima.

As a general rule, an adequate initial model ought to contain the long-wavelength structures of the investigated near-surface zone. Also, it should lead to simulated seismograms that limit the cycle skipping, particularly in the portions containing the fundamental mode. Unfortunately, in actual data cases such optimal initial models may be difficult to be obtained because of the lack of a priori information. To tackle this issue, we propose a new approach of Rayleigh-wave FWI with a global stochastic optimization based on genetic algorithms. Genetic algorithms (Stoffa and Sen, 1991; Sen and Stoffa, 1992; Mallick, 1995; Mallick, 1999) explore a wide model space to attain inversion outcomes and thus they are much less affected than local methods by

the presence of local minima. As a result, the importance of finding an adequate initial model is not as crucial as for local, gradient-based optimization methods.

Nonetheless, stochastic methods generally require huge computational resources especially when costly forward modeling is needed, leading to serious limitations in their practical applicability.

To attenuate this problem, we proceed as follows: (1) we parametrize the subsurface adopting a two-grid strategy (Sajeva et al., 2014, 2016; Aleardi and Mazzotti, 2017; Mazzotti et al., 2017), one coarse grid for the inversion phase and one fine grid for the modeling phase; (2) we make use of an offset-marching scheme and/or a frequency-marching scheme (Bunks et al., 1995) if deemed necessary; (3) we perform parallel computing (our code has been parallelized with Open MPI – C++). With these strategies adopted, the genetic-algorithm Rayleigh-wave FWI method that we propose can be used to derive near-surface Vs models even in cases where null a priori information is available.

We illustrate the proposed method starting from a brief description of the finite difference modeling (FDM) algorithm we use. Then, we introduce the two-grid strategy and the genetic-algorithm optimization. Finally, we discuss the results of three inversion tests, carried out without making use of any a priori information, on three synthetic examples that reproduce complex near-surface models. All the inversion tests have been performed assuming elastic wave propagation.

The application of the two-grid genetic-algorithm Rayleigh-wave FWI to two actual data sets, along with additional considerations required for field data inversion, is presented in a companion paper (Xing and Mazzotti, 2019).

METHOD

This section describes three key parts that construct our method. The first is the reliable simulation of Rayleigh waves. The second illustrates the two-grid scheme, which is quite important for reducing computational time. The third is the genetic-algorithm workflow.

Rayleigh-wave modeling

The engine that we employ for Rayleigh-wave modeling is a time-domain 2D elastic FDM code developed by Thorbecke and Draganov (2011) and further modified by Xing and Mazzotti (2016). We use the 2nd order approximation of derivatives in time and the 4th order approximation in space.

Convolutional perfectly matched layer (Roden and Gedney, 2000; Collino and Tsogka; 2001; Festa and Vilotte, 2005; Komatitsch and Martin, 2007; Gedney, 2011) is implemented in the modeling code to attenuate wave energy in the absorbing boundaries. The free surface condition recommended by Robertsson (1996) is used to simulate wave propagation in the presence of irregular topographic surfaces. To achieve a reliable simulation of Rayleigh waves, we suggest that the number of points (n) per minimum wavelength in the elastic FDM is set to 20 instead of to 5, which is the standard value for modeling body waves (Alford et al., 1974). The suggestion is based on our comparisons among results generated from various modeling codes and on

many tests in which *n* has been increased up to 100. This indication also coincides with that given in Nagai et al. (2005).

The value of 20 assigned to the number of points per minimum wavelength and the fact that Vs at the near surface is usually low, dictate that very fine grids should be used for modeling Rayleigh waves, thus making Rayleigh-wave modeling quite costly.

We checked the reliability of the employed FDM code by comparing its simulations on various reference models with the results of other modeling codes on the same models. The modeling results generated by the adopted 2D FDM code match well with seismograms from reflectivity modeling (Fuchs and Muller, 1971), spectral element modeling (SEM) (Komatitsch et al., 2001) and with seismograms provided by ENI employing another FDM code, confirming the reliability of the used forward modeling code.

The two-grid scheme

To reach satisfying results, a stochastic (global optimization) approach roughly requires a computing time that is exponentially proportional to the number of unknowns (Bellman, 1957). So does a genetic algorithm. In the FWI method we propose, the unknowns are the Vs, Vp and Rho at the nodes of the model grid. In the case of actual data (Xing and Mazzotti, 2018), the number of nodes in the modeling grid is usually tens of thousands. Such a huge number of grid nodes, triplicated, determines a number of unknowns which would require unacceptable computing time for a direct application of the genetic-algorithm Rayleigh-wave FWI.

The solution we propose to render the number of unknowns workable with the computing resources of standard computers is the adoption of a two-grid scheme. Figure 1 introduces the two-grid strategy. It shows a fine grid (black net) and the nodes (magenta dots) of a much coarser grid, superimposed on the Vs model pertaining to the 3rd synthetic example that we will discuss in detail later on. Only the portion of interest of the model is shown, but consider that absorbing boundaries are also present at the borders of the shown model.

The fine grid is used in forward modeling to guarantee the reliable computation of Rayleigh waves, so it follows the spacing criterion in FDM. Instead, the Vs, Vp and Rho at each node of the coarse grid constitute the unknowns, i.e. the total number of unknowns is three times the number of the nodes of the coarse grid. Therefore, it is on earth models parameterized with coarse grids that genetic-algorithm optimization is performed. The coarser the grid, the less the model resolution attained by the inversion, the less the required computing time. Although in Figure 1 the shown coarse grid is regular, practically it can be irregular or even random.

The choice of the coarse-grid dimensions depends on the available a priori information we may have, particularly on the minimum velocities of the subsurface and on the recorded maximum frequencies that could be recorded. With such information we could devise a grid whose spacing among the nodes is governed by the expected resolution, as can be roughly estimated making use of rules of thumb, such as that indicated by Park et al. (1999) for dispersion curve inversion. The grid node spacing can even be variable as a function of the (supposed) velocity variations. When no a priori

information is available, as it is the case we discuss here, the issue of how to parametrize the coarse grid model is inevitable: unless a transdimensional approach (Bodin et al., 2012) to the inversion is adopted, that is an approach where the number of unknowns is itself an unknown, the common practical choice is to design a regular grid with a reasonable number of nodes to maintain the computing times acceptable and, possibly, perform a second run with a more sophisticated grid designed on the basis of the provisional results.

We realize the conversion from the coarse-grid model to the correspondent fine-grid model by means of bilinear interpolation. Due to the long spacing among the nodes of the coarse grid and the smoothing effect of the interpolation, we usually obtain smooth predicted models reproducing only the long-wavelength structures of the subsurface. We name such predicted models “macro” models.

Genetic-algorithm full-waveform inversion with frequency and offset marching

Compared with local optimization methods, global optimization approaches are much less vulnerable to local minima and this is why we choose the genetic algorithm in the context of Rayleigh-wave FWI, which notoriously is a strong nonlinear problem. Additionally, different objective functions can be more easily implemented in global optimization methods.

The reason why we choose the genetic algorithm over other global optimization approaches is discussed in Sajeva et al. (2017). They compared the genetic algorithm with adaptive simulated annealing, particle swarm optimization and the neighborhood algorithm. They found that in the context of both analytical objective functions and of 1D elastic FWI, the genetic algorithm outperformed the others. Moreover, the genetic algorithm is naturally parallelizable, which is particularly important in our case for speeding up computation.

Genetic algorithms imitate the biological-evolution process to realize optimization. Figure 2 displays the workflow of our genetic-algorithm FWI. The mechanism of the inversion is as follows.

The first step is the creation of the initial population, which in our case is an ensemble of Vs, Vp and density (Rho) models. The randomly created models (individuals) are uniformly distributed within predefined search ranges that limit the model space to be explored by the algorithm. The user can establish such search ranges on the basis of deductions on the observed data (e.g. on dispersion spectra) or on some kind of a priori information on the investigated zone, when available.

Next, a synthetic seismogram is computed by forward modeling for each model of the initial population. Based on a user-defined objective function, data misfits between observed data and simulated data are calculated for the evaluation of the model fitness in order to sift out the promising models, which are then paired to produce offspring by combination and mutation. Combination here means exchanging part of values (that is, velocities and densities at some of the grid nodes) of paired models, while mutation is randomly changing within the predefined search ranges a small portion of values of selected models.

After that, the models leading to minor data misfits in the offspring are inserted back to the original population to replace the models associated with larger data misfits. At each generation, selection, recombination, mutation, and reinsertion are performed to obtain models with ever-decreasing data misfits. This indicates that, theoretically, the data misfits can always be improved until the ideal one is found. In practice, considering efficiency, a stopping criterion, such as a predefined maximum generation or a threshold on the data misfit, is set to terminate the inversion.

The forward modeling, which is performed between the creation (or reinsertion) of models and the evaluation of the objective function, requires most of the computational time.

As shown in Figure 2, frequency (Bunks et al., 1995) and offset (Masoni et al., 2016) marching is embedded in the inversion workflow for the further avoidance of cycle skipping. Below we list the main controlling parameters (Pohlheim, 2006) of the genetic algorithm we use. The correct setting of the parameters is empirical and is strongly influenced by the number of unknowns. In the list, we also indicate the settings adopted

in all the inversion tests shown in this and in the accompanying paper. Our choices were based on several tests and on previous works (Sajeva et al., 2014, 2016; Aleardi and Mazzotti, 2017; Mazzotti et al., 2017; Xing and Mazzotti, 2017a, b).

- Number of individuals. It is the number of subsurface models that form the population. The higher this number, the more thorough the exploration of the model space. With approximately 200 unknowns (Vs, Vp and Rho at the nodes of the coarse model grid), the number of individuals we set was 2000.
- Number of sub-populations. It is the number of groups that population (models) is divided into so as to simulate biological migration. We adopted 5 sub-populations. In our case migration means moving a percentage of models from one to other sub-populations. Recombination in Figure 2 occurs for inter-population.
- Maximum generation. It is the number of generations evolved before the inversion outcome is obtained and we set it to 200.

- Selection rate. It is the percentage of the models (individuals) that are chosen to be paired for generating models of the next generation (offspring). We set this parameter to 0.8.
- Selection pressure. It is the ratio between the probability that more promising models, namely the models associated with relatively smaller data misfits, are selected and the probability that any model is chosen. In our tests it changed linearly from 1 to 2 along generations.
- Mutation rate. It is the probability that a model is mutated and we set it to 0.1.
- Reinsertion rate. It is the percentage of the offspring that replace the less promising individuals (models) in the original population to form the new population. 0.6 was the setting we chose.
- The 1st generation of migration. It is the number of the generation at which migration occurs at the 1st time. We set it to 30.
- Migration interval. It is the number of the generations between two successive migrations. In our tests it was set to 20.

- Migration rate. It is the percentage of the models that are allowed to migrate. 0.2 was the value we adopted.

The values of the controlling parameters were chosen considering the balance between inversion results and computational time. For instance, if we increase the number of individuals, the exploration of the model space will be more thorough at the expense of higher computing costs. Conversely, if we decrease the selection rate, we may attain a faster convergence and save computing time, but we increase the risk of reaching a premature convergence and being stuck in a local minimum.

According to our experience, with the proposed genetic-algorithm FWI, depending on the selected coarse grid spacing, we are able to derive final model predictions or provide adequate initial models for Rayleigh-wave FWI with local optimization techniques for further refinements (Xing et al., 2018).

In what follows, we show the application of our FWI to three synthetic examples. Instead, for checking the application of the method to actual Rayleigh-wave data, along

with the additional considerations demanded for the practical use of the method, readers can refer to our companion paper.

SYNTHETIC EXAMPLES

We aim at demonstrating that the proposed method is able to fairly predict near-surface Vs models from Rayleigh waves, even in the case that no a priori information is given. In this section, we first present the reference models. Then, we show the inversion specifications. Finally, we illustrate the predicted Vs models and seismograms together with the evolution of data and model misfits.

Reference models

The reference models that we employed in the three tests are displayed in Figure 3. Only Vs models are shown due to the well-known fact that Rayleigh waves are mostly sensitive to Vs, consequently Vs is the most important parameter that can be retrieved by Rayleigh-wave inversion.

The 1st model (Figure 3a) is a 1D model with strong velocity contrasts and with velocity inversions in the 2nd and in the 4th layers. This kind of layering is generally considered as difficult to be inverted for by existing Rayleigh-wave inversion techniques (Cercato, 2009, among others). This seems to be confirmed by some test we carried out employing dispersion curve inversion with no or with scarce a priori information. One of the reasons is that the velocity inversions prevent the generation of head waves and consequently make it difficult to build suitable initial models by approaches such as first break tomography.

The 2nd model (Figure 3b) is a 2D model with strong lateral variations: at the depth of, say, 6 m, at the lateral coordinate 20 m, the lateral velocity contrast amounts to 200 m/s. This “anticlinal” structure violates the 1D assumption that is common in dispersion curve inversion, which makes it difficult to be inverted for via that method.

The 3rd model (Figure 3c), besides the lateral velocity variation at depth, shows an irregular topographic surface which further distantiates the model from 1D geometry. Moreover, the different elevations of sources and of receivers will result in the distortion

of the “observed” data and will likely produce diffractions. Intuitively, the increased complexity will make the data more vulnerable to the local-minimum problem (Bunks et al., 1995; Cercato, 2011).

We carried out the synthetic tests committing an inversion “crime”, that is, the “observed” data were computed by using the same forward-modeling engine employed in our inversion code and source wavelets were known.

The acquisition geometry was the same for all the three tests. Following the lead of engineering studies where, in applying techniques such as MASW, only few shots are generally employed, three shot gathers, of which one is split-spread and two are off-ends, with evenly spaced receivers, were the input data for the inversion. The blasts and reverse triangles in Figure 3 symbolically illustrate the positions of the sources and receivers, which were placed on the topographic surface. The source to receiver offsets ranged from 4.25 m to 32 m.

To test the impact of background noise, weak random noise was added to the simulated "observed" data in the 1st example.

Inversion specifications

The same inversion specifications were set for the three tests.

Since we simulated the case where no a priori information was available, the genetic-algorithm search ranges were constant with depth and with lateral position. Search ranges limit the model space that can be explored by the genetic algorithm and thus it is recommendable to use a relatively large search range when no a priori information can suggest a restriction. Therefore, we set the search ranges for Vs, Vp and Rho as 100 – 500 m/s, 500 – 900 m/s and 1350 – 1750 kg/m^3, respectively.

Data misfits χ were calculated by the L1 norm, which is less vulnerable (Kwak, 2008) to outliers compared with the L2 norm, between observed data and predicted data

$$\chi = \frac{\sum_{n_x=1}^{N_x}\sum_{n_t=1}^{N_t}|\boldsymbol{D}_{n_t,n_x} - \boldsymbol{P}_{n_t,n_x}|}{\sum_{n_x=1}^{N_x}\sum_{n_t=1}^{N_t}|\boldsymbol{D}_{n_t,n_x}|}, \#(1)$$

where $\boldsymbol{D}$ and $\boldsymbol{P}$ are respectively the "observed" and predicted data, n_t and n_x are respectively the time and trace sampling number, N_t and N_x are respectively the total number of time samples and of traces. In the tests, the total misfit was a summation over all the three shots.

We made use of the offset-marching strategy and we started the inversion with the near-offset data until the offset of 9 m. Then, we gradually included in the inversion the data at larger offsets, until 12 m, 15 m, 20 m, 26 m and 32 m. Given the minimum velocity defined in the search ranges and the inverted maximum frequency, which were the same for all the three examples, the modeling grid was composed of 5289 nodes to guarantee an appropriate grid spacing. The coarse grids for the inversion were defined simulating the case where no a priori information could suggest a particular geometry of the grids, thus they were set as regularly spaced. In the two flat-topography examples, we defined the same coarse inversion grid of 45 nodes, which brought to 135 unknowns to be inverted for. Instead, in the test with the 2D irregular-topography model, due to the

plain fact that the part above the surface was not to be inverted for, the coarse grid was built with 39 nodes that led to 117 unknowns.

The other parameters related to the genetic algorithm, such as the number of individuals and the maximum generation, were set as the empirical values listed in the *Method* section.

The tests were carried out on a distributed computing system made of computers with two cores. Each core had 20 threads. Using 1 thread, each forward simulation took about 2s. Employing 545 threads, each inversion took about 1 hour.

Inversion outcomes

In this part, we show that fair inversion outcomes can be obtained by applying the two-grid genetic-algorithm FWI method, even though in the tests (1) complex near-surface models have been considered, (2) coarse inversion grids have been used, and (3) no a-priori information has been exploited. The predicted Vs models are displayed in Figure 4, while the 1D Vs vertical profiles at the lateral distance of 4 m are presented in

Figure 5 to allow for a more detailed comparison. The best predicted seismograms, along with the "observed" data, are exhibited in Figure 6. An example of the evolution of the data and model misfits is given in Figure 7.

Concerning the 1st test on the 1D model (Figure 3a), we can see that the main subsurface features have been recovered (although with moderately different velocities) by the inversion (Figure 4a). Despite the fact that the search ranges had been set constant with depth, the two velocity inversions located at the 2nd and at the 4th (bottom) layer have been detected and the prediction of their depth positions is acceptable. Obviously, sharp interfaces cannot be reproduced owing to the adopted parameterization of the subsurface. It appears that the random noise added to the "observed" data has not influenced the results.

The model prediction for the 2D-model test is shown in Figure 4b and should be compared with the reference model in Figure 3b. The long-wavelength structures have been predicted, particularly the "anticlinal" form on the right and the general increase of velocities with depth. The predicted model does not fully coincide with the reference

model, but this is expected due to the coarseness of the inversion grid and, likely, illumination problems at the edges of the model.

The inversion result of the 3rd example, the one with an irregular-topography model, is shown in Figure 4c. Again, the main structure of the reference model (Figure 3c) has been recovered even in the shallowest part and the transition from low velocities to deeper and laterally varying higher velocities is quite distinguishable.

A more detailed assessment of the results can be made on the 1D Vs profiles shown in Figure 5. The dashed cyan lines indicate the search ranges set in the inversion. Note that the search ranges are wide and constant, that is they do not follow the Vs trends of the reference models. Notwithstanding that, all the predicted velocity trends seem to be a low-frequency reproduction of the actual trends. Although the velocity values of the reference and of the predicted models do not coincide, the inversion seems to be able to detect the velocity changes (particularly the velocity inversions in the 1st example).

Coming to the comparison between observed and predicted data, Figure 6 shows the three sets of shot gathers, separated by dashed cyan lines, with observed traces represented in black and predicted traces in red. All the seismograms have been normalized trace by trace. Figure 6a illustrates the case of the 1st example. Although the observed data have been contaminated by weak random noise (S/N ratio equal to 30.7dB), the predicted data fairly match the observed data along the whole range of offsets. The same conclusion can be drawn also for the other two examples shown in Figures 6b and 6c. Note that in Figure 6c, the complex distortions of the observed wave-train caused by the irregular topographic surface have been well reproduced in the simulated data.

As a further check, we present in Figure 7 the evolution along the genetic-algorithm generations of the data misfit and of the Vs, Vp and Rho model misfits pertaining to the 3rd example. The evolution of the misfits in the other 2 examples are not exhibited as they show the same characters. The black curves indicate the minimum data misfit at each generation in Figure 7a, while in Figure 7b, c and d they indicate the

misfit of the model associated with the seismogram giving the minimum data misfit. The red curves in Figure 7 are, sequentially, the mean misfits computed over the entire population of simulated seismograms (Figure 7a) and their respective models of Vs, Vp and Rho (Figures 7b, c and d). The dashed cyan lines delineate the offset-marching frame. The blue annotations indicate the offset ranges of the inverted data at each offset-marching phase.

In Figure 7a we can observe that within each offset-marching phase the minimum as well as the mean data misfits tend to rapidly decrease, which is encouraging. At generations when an offset-marching transition occurs, the absolute data misfit will likely increase because the data can be pretty different before and after the addition of an offset range. However, from the plot in Figure 7a, we can assess the evolution of the data misfit only within each offset range, but we cannot make any comparison among the data misfit values within different offset ranges due to the fact that the observed data that are the normalization factor in the objective function of equation 1, change with offset range. At the last (200^{th}) generation of the inversion, the

mean data misfit is very close to the minimum data misfit. Combined with the fairly predicted data in Figure 6c, this closeness indicates that the space for a further reduction of the data misfit is limited.

The evolution of the Vs-model misfit (Figure 7b), although generally decreasing, shows significant oscillations that are a consequence of the strong nonlinearity of the Rayleigh-wave inversion. We use the term “best” model misfits to indicate the misfits of the models that give rise to the minimum data misfits. Encouragingly, despite the ambiguity, in Figure 7b both the best Vs-model misfits and the mean Vs-model misfits show a general decrease with generations. At the last (200^{th}) generation, the mean Vs-model misfit is slightly larger than the best Vs-model misfit, but the two misfits are quite near, indicating that the “best” and the mean model are likely very similar. This is indeed demonstrated by Figure 8 where the mean models for all the previous examples are shown. The reason for the similarity between best models and mean models is the continuous loss of the variety in the population along generations as a consequence of selection and recombination.

Concerning the estimation of Vp and Rho models, Figures 7c and d show their respective evolution. It is immediately evident the effect of the minor sensitivity of the data to Vp and Rho. In fact, although we observe a general improvement of both the best Vp-model misfit and the best Rho-model misfit (black curves in Figures 7c and d) along generations, the rate of the improvement is significantly lower than that for Vs models. Also, Vp and Rho models associated with the best seismograms may show misfits which are much greater than the mean model misfits at the same generation. This is again a consequence of the less control that Vp and Rho exercise on the observed Rayleigh waves: the average of a certain number of - somewhat erratic - Vp and Rho models, may be more similar to the reference model than the model associated with the best seismogram. This is why, according to our inversion tests, unless a priori information is included, we can rarely obtain Vp or Rho models with correct structures. In fact, the Vp and Rho models retrieved in the present tests are far from reproducing the true models.

CONCLUSIONS

We have proposed a two-grid Rayleigh-wave FWI via a genetic-algorithm optimization. A two-grid scheme, which limits the number of unknowns so as to decrease significantly the computational time, has been adopted for the practical applicability of the method. The proposed inversion fairly predicts the long-wavelength components of near-surface Vs models, confirming the ability of genetic algorithms to converge even when no a priori information is available.

Among the many tests that had been performed, we have shown here the results pertaining to three synthetic models that are generally considered as being fairly complex to be inverted for by means of dispersion curve inversion or by FWI with local optimization techniques, without a priori information. The three models individually contain (1) strong velocity contrasts and velocity inversions, (2) strong lateral velocity variations and (3) an irregular topographic surface.

Though quite coarse inversion grids had been used, so that the reconstructed models can only be low-resolution models, in the 1st test with the 1D model the two velocity decreases have been correctly detected, while in the 2nd and 3rd examples both

the lateral velocity variations and the effects of the irregular topography have been fairly reproduced.

Because of the fair reproduction of the macro structures of the reference models and the adequate match of predicted and “observed” seismograms, the models obtained by our stochastic method are supposed to be suitable input to Rayleigh-wave FWI through local optimization techniques for further refinement, if needed. Preliminary tests carried out employing the IFOS2D, a gradient-based FWI code developed by the TOAST (Toolbox for applied seismic tomography) project (Bohlen, 2002; Köhn et al., 2012; Groos et al., 2014), seem to confirm the expectations.

As all the models explored by the genetic algorithm can be collected, we can also think of expressing the results not just as the best model or the mean model, but as frequency histograms which could be further elaborated to retrieve probability distributions. This would allow for the parallel estimation of uncertainties associated with the most likely model. However, this approach remains among the works to be done for Rayleigh-wave FWI. Instead, a work that has been done is the application of the

proposed method to two field data cases. The results are presented in a companion paper, along with the discussion on the practical issues that need be accordingly addressed.

ACKNOWLEDGEMENTS

Thanks are due to the unknown reviewers for their suggestions and constructive comments. We gratefully acknowledge Dr. Michele Buia of ENI for providing us the results of their finite difference modeling to be compared with our synthetic seismograms.

APPENDIX A

3D to 2D correction

In the real world, wavefronts are spherical while in the 2D FDM, the source is a line source that gives rise to cylindrical wave propagation. To make field data (or modeled 3D data) and our 2D modeling outcomes comparable, we correct the former via a 3D to 2D correction technique proposed by Forbriger et al. (2014).

Following Forbriger et al. (2014) and Schäfer et al. (2014), we apply the multilayer surface-wave transformation to the 3D data, with the exception of the near-offset traces where the single-layer transformation is used instead.

Below is the algorithm for the multilayer surface-wave transformation.

(1) Convolve the data with $\sqrt{t^{-1}}$ where t is the time.

(2) Multiply the data with $r\sqrt{2t^{-1}}$ where r is the source-receiver distance.

The algorithm for the single-layer transformation is as follows:

(1) Convolve the data with $\sqrt{t^{-1}}$.

(2) Multiply the data with $\sqrt{2rV_{ph}}$ where V_{ph} is the single phase velocity.

We checked the effectiveness of the adopted correction method on the basis of two near-surface models shown in Figure B-1. The first model (Figure B-1a) is a quite complex near-surface model that contains sharp velocity contrasts and strong velocity

inversions. The second model (Figure B-1b) is a realistic model derived from an actual borehole.

The reflectivity modeling results of the two models are shown in Figure B-2, with the black traces indicating the seismograms simulated via a 3D wave propagation, and the red traces representing the 3D to 2D corrected seismograms. For the seismograms of both models, the phase correction is particularly evident although a significant amplitude correction has also been performed but its effect is less visible due to the trace by trace normalization.

In Figure B-3, the reflectivity modeling results with the 3D to 2D correction applied are displayed as the black seismograms, while the 2D elastic FDM outcomes are presented as the red seismograms. The results for both models show very satisfactory matching between FDM traces and 3D to 2D corrected reflectivity traces at all offsets.

In the perspective of Rayleigh-wave FWI, the application of the 3D to 2D correction, whose effectiveness is confirmed by the quite good match between the 2D FDM seismograms and the 3D to 2D corrected reflectivity seismograms, will assure more correct model predictions.

REFERENCES

Aleardi, M., and A. Mazzotti, 2017, 1D elastic full-waveform inversion and uncertainty estimation by means of a hybrid genetic algorithm – Gibbs sampler approach: Geophysical Prospecting, **65**, 64-85, doi: 10.1111/1365-2478.12397.

Alford, R. M, K. R. Kelly, and D. M. Boore, 1974, Accuracy of finite-difference modeling of the acoustic wave equation: GEOPHYSICS, **39**, 834-842, doi: 10.1190/1.1440470.

Bellman, R. E., 1957, Dynamic programming: Princeton University Press.

Bodin, T., M. Sambridge, H. Tkalčić, P. Arroucau, K. Gallagher, and N. Rawlinson, 2012, Transdimensional inversion of receiver functions and surface wave

dispersion: JOURNAL OF GEOPHYSICAL RESEARCH, **117**, B02301, 1-24, doi: 10.1029/2011JB008560.

Bohlen, T., 2002, Parallel 3-D viscoelastic finite difference seismic modeling: Computers & Geosciences, 28, 887-899, doi: 10.1016/S0098-3004(02)00006-7.

Bohlen, T., S. Kugler, G. Klein, and F. Theilen, 2004, 1.5D inversion of lateral variation of Scholte-wave dispersion: GEOPHYSICS, **69**, 330-344, doi: 10.1190/1.1707052.

Brossier, R., S. Operto, and J. Virieux, 2009, Seismic imaging of complex onshore structures by 2D elastic frequency-domain full-waveform inversion: GEOPHYSICS, **74**, no. 6, WCC105-WCC118, doi: 10.1190/1.3215771.

Bunks, C., F. M. Saleck, S. Zaleski, and G. Chavent, 1995, Multiscale seismic waveform inversion: GEOPHYSICS, **60**, 1457-1473, doi: 10.1190/1.1443880.

Cercato, M., 2009, Addressing non-uniqueness in linearized multichannel surface wave inversion: Geophysical Prospecting, **57**, 27–47, doi: 10.1111/j.1365-2478.2007.00719.x.

Cercato, M., 2011, Global surface wave inversion with model constraints: Geophysical Prospecting, **59**, 210–226, doi: 10.1111/j.1365-2478.2010.00922.x.

Collino, F., and C. Tsogka, 2001, Application of the perfectly matched absorbing layer model to the linear elastodynamic problem in anisotropic heterogeneous media: GEOPHYSICS, **66**, 294-307, doi: 10.1190/1.1444908.

Festa, G., and J. Vilotte, 2005, The Newmark Scheme as Velocity-Stress Time Staggered: An Efficient PML Implementation for Spectral Element Simulations of Electrodynamics: Geophys. J. Int., **161**, 789–812, doi: 10.1111/j.1365-246X.2005.02601.x.

Forbriger, T., 2003a, Inversion of shallow-seismic wavefields: I. Wavefield transformation: Geophys. J. Int., **153**, 719–734, doi:10.1046/j.1365-246X.2003.01929.x.

Forbriger, T., 2003b, Inversion of shallow-seismic wavefields: II. Inferring subsurface properties from wavefield transforms: Geophys. J. Int., **153**, 735–752, doi: 10.1046/j.1365-246X.2003.01985.x.

Forbriger, T., L. Groos, and M. Schäfer, 2014, Line-source simulation for shallow-seismic data. Part 1: theoretical background: Geophys. J. Int., **198**, 1387-1404, doi: 10.1093/gji/ggu199.

Fuchs, K., and G. Muller, 1971, Computation of synthetic seismograms with the reflectivity method and comparison with observations: Geophys. J. R. astr. Soc., **23**, 417-433, doi: 10.1111/j.1365-246X.1971.tb01834.x.

Gedney, S. D., 2011, Introduction to the finite-difference time-domain (FDTD) method for electromagnetics: Morgan & Claypool Publishers, doi: 10.2200/S00316ED1V01Y201012CEM027.

Groos, L., M. Schäfer, T. Forbriger, and T. Bohlen, 2014, The role of attenuation in 2D full-waveform inversion of shallow-seismic body and Rayleigh waves: GEOPHYSICS, **79**, no. 6, R247–R261, doi: 10.1190/GEO2013-0462.1.

Groos, L., M. Schäfer, T. Forbriger, and T. Bohlen, 2017, Application of a complete workflow for 2D elastic full-waveform inversion to recorded shallow-seismic Rayleigh waves: GEOPHYSICS, **82**, no. 2, R109-R117, doi: 10.1190/geo2016-0284.1.

Köhn, D., D. De Nil, A. Kurzmann, A. Przebindowska, and T. Bohlen, 2012, On the influence of model parametrization in elastic full waveform tomography: Geophys. J. Int., **191**, 325–345, doi: 10.1111/j.1365-246X.2012.05633.x.

Komatitsch, D., R. Martin, J. Tromp, M. A. Taylor, and B. A. Wingate, 2001, Wave propagation in 2-D elastic media using a spectral element method with triangles and quadrangles: Journal of Computational Acoustics, **9**, 703-718, doi: 10.1142/S0218396X01000796.

Komatitsch, D., and R. Martin, 2007: An unsplit convolutional perfectly matched layer improved at grazing incidence for the seismic wave equation: GEOPHYSICS, **72**, no. 5, SM155-SM167, doi: 10.1190/1.2757586.

Kwak, N., 2008, Principal component analysis based on L1-norm maximization: IEEE Trans. Pattern Anal. Mach. Intell., 30,1672–1680, doi: 10.1109/TPAMI.2008.114.

Mallick, S., 1995, Model-based inversion of amplitude-variations-with-offset data using a genetic algorithm: GEOPHYSICS, **60**, 939-954, doi: 10.1190/1.1443860.

Mallick, S., 1999, Some practical aspects of prestack waveform inversion using a genetic algorithm: An example from the east Texas Woodbine gas sand: GEOPHYSICS, **64**, 326-336, doi: 10.1190/1.1444538.

Maraschini, M., F. Ernst, S. Foti, and L. V. Socco, 2010, A new misfit function for multimodal inversion of surface waves: GEOPHYSICS, **75**, no. 4, G31-G43, doi: 10.1190/1.3436539.

Masoni, I., R. Brossier, J. Virieux, and J. L. Boelle, 2014, Robust full waveform inversion of surface waves: SEG Technical Program, Expanded Abstracts, 1126-1130, doi: 10.1190/segam2014-1077.1.

Masoni, I., J. L. Boelle, R. Brossier, and J. Virieux, 2016, Layer stripping FWI for surface waves: SEG Technical Program, Expanded Abstracts, 1369-1373, doi: 10.1190/segam2016-13859781.1.

Mazzotti, A., N. Bienati, E. Stucchi, A. Tognarelli, M. Aleardi, and A. Sajeva, 2017, Two-grid genetic algorithm full-waveform inversion: The Leading Edge, **35**, 1068-1075. doi: 10.1190/tle35121068.1.

Nagai, K., A. O'Neill, Y. Sanada, and Y. Ashida, 2005, Genetic Algorithm Inversion of Rayleigh Wave Dispersion from CMPCC Gathers Over a Shallow Fault Model: JEEG, **10**, 275-286, doi: 10.2113/JEEG10.3.275.

Park, C. B., R. D. Miller, and J. H. Xia, 1999, Multichannel analysis of surface waves: GEOPHYSICS, **64**, 800-808, doi: 10.1190/1.1444590.

Pohlheim, H., 2006, Evolutionary algorithms: overview, methods and operators, http://www.geatbx.com/download.html, accessed 24 January 2018.

Rix, G. J., 2004, Near-surface site characterization using surface waves, *in* C. G. Lai, and K. Wilmański, eds., Surface waves in geomechanics: direct and inverse modeling for soils and rocks: CISM International Centre for Mechanical Sciences 481, 1-46, doi: 10.1007/3-211-38065-5_1.

Robertsson, J. O. A., 1996, A numerical free-surface condition for elastic/viscoelastic finite-difference modeling in the presence of topography: GEOPHYSICS, **61**, 1921-1934, doi: 10.1190/1.1444107.

Roden, A., and S. D. Gedney, 2000, Convolutional PML (CPML): an efficient fdtd implementation of the CFSPML for arbitrary media: Microwave and Optical Technical Letter, **27**, 334-339, doi: 10.1002/1098-2760(20001205)27:5<334::AID-MOP14>3.0.CO;2-A.

Sajeva, A., M. Aleardi, A. Mazzotti, N. Bienati, and E. Stucchi, 2014, Estimation of velocity macro-models using stochastic full-waveform inversion: SEG Technical Program, Expanded Abstracts, 1227-1231, doi: 10.1190/segam2014-1088.1.

Sajeva, A., M. Aleardi, E. Stucchi, N. Bienati, and A. Mazzotti, 2016, Estimation of acoustic macro models using a genetic full-waveform inversion: applications to the Marmousi model: GEOPHYSICS, **81**, no. 4, R173-R184, doi: 10.1190/geo2015-0198.1.

Sajeva, A., M. Aleardi, B. Galuzzi, E. Stucchi, E. Spadavecchia, and A. Mazzotti, 2017, Comparing the performances of four stochastic optimisation methods using analytic objective functions, 1D elastic full-waveform inversion, and residual static computation: Geophysical Prospecting, **65**, 322–346, doi: 10.1111/1365-2478.12532.

Schäfer, M., L. Groos, T. Forbriger, and T. Bohlen, 2013, 2D full waveform inversion of recorded shallow seismic Rayleigh waves on a significantly 2D structure: Near Surface Geoscience Technical Program, Expanded Abstracts, doi: 10.3997/2214-4609.20131338.

Schäfer, M., L. Groos, T. Forbriger, and T. Bohlen, 2014, Line-source simulation for shallow-seismic data. Part 2: full-waveform inversion—a synthetic 2-D case study: Geophys. J. Int., **198**, 1405-1418, doi: 10.1093/gji/ggu171.

Sen, M. K., and P. L. Stoffa, 1992, Rapid sampling of model space using genetic algorithms: examples from seismic waveform inversion: Geophys. J. Int., **108**, 281-292, doi: 10.1111/j.1365-246X.1992.tb00857.x.

Socco, L. V., and C. Strobbia, 2004. Surface-wave method for near-surface characterisation: A tutorial: Near Surface Geophysics, **2**, 165–185, doi: 10.3997/1873-0604.2004015.

Socco, L. V., S. Foti, and D. Boiero, 2010, Surface-wave analysis for building near-surface velocity models — Established approaches and new perspectives: GEOPHYSICS, **75**, no. 5, 75A83-75A102, doi: 10.1190/1.3479491.

Stoffa, P. L., and M. K. Sen, 1991, Nonlinear multiparameter optimization using genetic algorithms: Inversion of plane‐wave seismograms: GEOPHYSICS, **56**, 1794-1810, doi: 10.1190/1.1442992.

Thorbecke, J. W., and D. Draganov, 2011, Finite-difference modeling experiments for seismic interferometry: GEOPHYSICS, **76**, no. 6, H1-H18, doi: 10.1190/geo2010-0039.1.

Tran, K. T., M. McVay, M. Faraone, and D. Horhota, 2013, Sinkhole detection using 2D full seismic waveform tomography: GEOPHYSICS, **78**, no. 5, R175-R183, doi: 10.1190/geo2013-0063.1.

Xia, J. H., R. D. Miller, and C. B. Park, 1999, Estimation of near-surface shear-wave velocity by inversion of Rayleigh waves: GEOPHYSICS, **64**, 691-700, doi: 10.1190/1.1444578.

Xing, Z., and A. Mazzotti, 2016, Rayleigh wave modeling complexities in the perspective of full waveform inversion of surface waves – synthetic examples: Near

Surface Geoscience Technical Program, Expanded Abstracts, doi: 10.3997/2214-4609.201601909.

Xing, Z., and A. Mazzotti, 2017a, Two-grid full waveform Rayleigh wave inversion by means of genetic algorithm with frequency marching: EAGE Technical Program, Expanded Abstracts, doi: 10.3997/2214-4609.201701412.

Xing, Z., and A. Mazzotti, 2017b, Surface wave FWI on complex models: the robustness of the inversion to assumptions and forward modeling approximations: Near Surface Geoscience Technical Program, Expanded Abstracts, doi: 10.3997/2214-4609.201702019.

Xing, Z., and A. Mazzotti, 2018, Two-grid genetic algorithm full waveform inversion of surface waves: two actual data examples: EAGE Technical Program, Expanded Abstracts, doi: 10.3997/2214-4609.201801375.

Xing, Z., F. Rappisi, and A. Mazzotti, 2018, A new workflow for surface wave FWI combining genetic algorithm and gradient-based optimization algorithms: Near Surface

Geoscience Technical Program, Expanded Abstracts, doi: 10.3997/2214-4609.201802567.

Xing, Z., and A. Mazzotti, 2019, Two-grid full-waveform Rayleigh-wave inversion via a genetic algorithm: part 2 – application to two actual data sets: submitted to Geophysics.

LIST OF FIGURES

1 An example of the two-grid scheme. The black grid indicates the fine modeling grid that guarantees the reliable modeling of Rayleigh waves. The magenta dots denote the coarse inversion grid. A bilinear interpolation converts the coarse-grid model into its correspondent fine-grid model. The background colors refer to the Vs model of the 3rd example. In the figure only the portion of the model which is of interest is exhibited, that is, the absorbing boundaries to be added in modeling are not shown here.

2 The workflow of our genetic-algorithm FWI. Frequency and offset marching have been embedded in the workflow to further avoid cycle skipping.

3 Reference near-surface Vs models: (a) 1D model with sharp velocity contrasts and inversions; (b) 2D model with strong lateral velocity variations; (c) 2D model with an irregular topographic surface and lateral velocity variations. The blasts and reverse triangles on the topographic surfaces illustrate the locations of the sources and receivers used in the inversions.

4 The predicted Vs models corresponding to the best seismograms (minimum data misfits): (a) 1D model; (b) 2D model; (c) 2D irregular-topography model. The dashed magenta lines indicate the positions of the 1D Vs profiles that will be presented in Figure 5. Note that the long-wavelength structures of the reference models (Figure 3) have been fairly reproduced.

5 The Vs profiles picked from the reference (Figure 3) and predicted (Figure 4) models at the lateral distance of 4 m. From (a) to (c) the profiles sequentially correspond with the 1D model, the 2D model and the 2D irregular-topography model. The profiles picked from the reference models are drawn in gray while those picked from the predicted models are presented in blue. The dashed cyan lines show the Vs search ranges in our genetic-algorithm FWI. Note that the search ranges are wide and constant, that is, they do not follow the trends of the reference Vs profiles, and that the predicted Vs profiles fairly match the reference model profiles.

6 The “observed” (black traces) and predicted (red traces) best seismograms related to the (a) 1D model, (b) 2D model and (c) 2D irregular-topography model. One every six traces is plotted. The observed seismograms in (a)

have been contaminated with weak random noise. The dashed cyan lines delimit the left, middle and right shot gathers. The seismograms have been normalized trace by trace. The matching between observed and predicted seismograms is quite good at all offsets.

7 The evolution of the data and model misfits for the 3rd example: (a) data misfits; (b) Vs-model misfits; (c) Vp-model misfits; (d) Rho-model misfits. The black and red curves in (a) indicate the minimum data misfits and the mean data misfits, respectively. In (b), (c) and (d) the black curve shows the misfits of the Vs, Vp and Rho models associated with the seismograms giving the minimum data misfits (best seismograms), while the red curve represents the misfits of the mean models calculated over the entire population. The blue annotations delimited by the dashed cyan lines indicate the offset ranges of the data inverted at each phase of the offset-marching frame.

8 The mean of the Vs models at the last generations of our genetic-algorithm Rayleigh-wave FWI: (a) 1D model; (b) 2D model; (c) 2D irregular-

topography model. These mean models are rather similar to the best models presented in Figure 4.

B-1 Models used for checking the effectivity of the adopted 3D to 2D correction (Forbriger et al., 2014) method. (a) A synthetic model that contains sharp velocity contrasts and velocity inversions. (b) A realistic model derived from three-component down-hole recordings and density log.

B-2 Reflectivity modeling results of (a) the model in Figure B-1a and (b) the model in Figure B-1b. The black and red seismograms are the reflectivity modeling outcomes before and after the application of the 3D to 2D correction, respectively. The seismograms have been normalized trace by trace. The phase differences are evident at the whole offset range.

B-3 Modeling outcomes of (a) the model in Figure B-1a and (b) the model in Figure B-1b. The black seismograms are the results of reflectivity modeling with the 3D to 2D correction applied, while the red seismograms are outcomes of the employed 2D FDM code. The seismograms have been normalized trace by trace. In

both (a) and (b), the black and red seismogram satisfactorily match, even at the farthest offset.

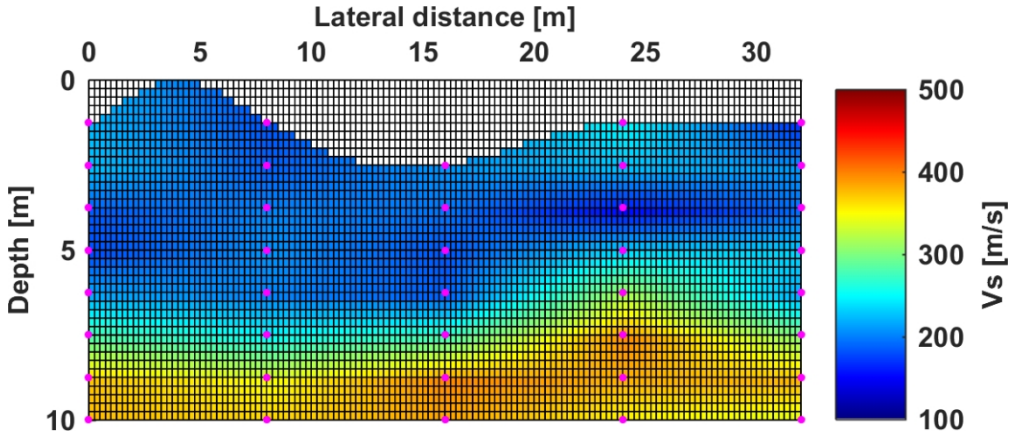

Figure 1. An example of the two-grid scheme. The black grid indicates the fine modeling grid that guarantees the reliable modeling of Rayleigh waves. The magenta dots denote the coarse inversion grid. A bilinear interpolation converts the coarse-grid model into its correspondent fine-grid model. The background colors refer to the Vs model of the 3rd example. In the figure only the portion of the model which is of interest is exhibited, that is, the absorbing boundaries to be added in modeling are not shown here.

100x42mm (300 x 300 DPI)

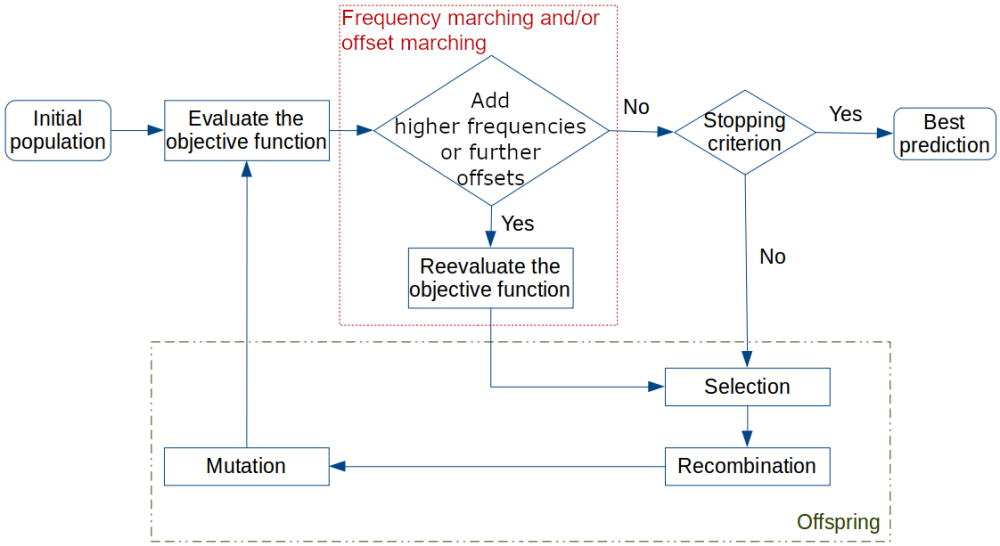

Figure 2. The workflow of our genetic-algorithm FWI. Frequency and offset marching have been embedded in the workflow to further avoid cycle skipping.

94x51mm (300 x 300 DPI)

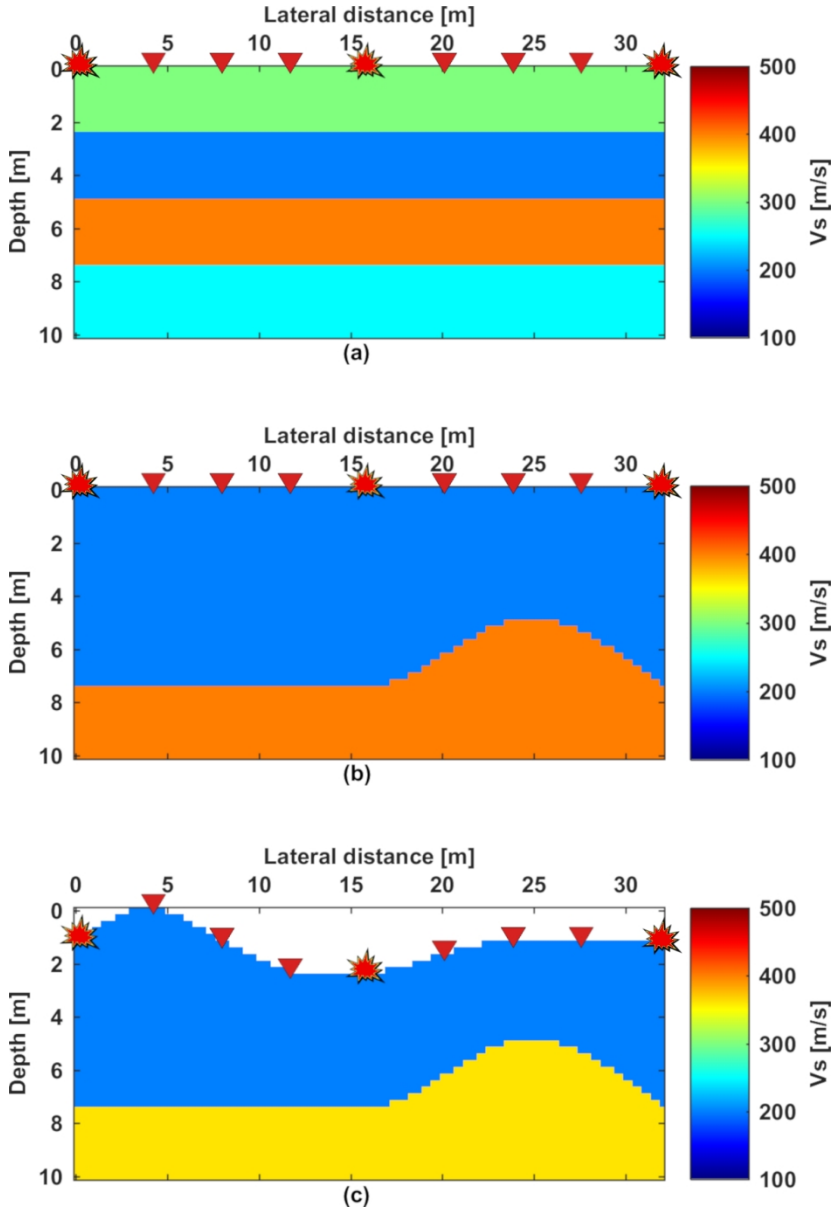

Figure 3. Reference near-surface Vs models: (a) 1D model with sharp velocity contrasts and inversions; (b) 2D model with strong lateral velocity variations; (c) 2D model with an irregular topographic surface and lateral velocity variations. The blasts and reverse triangles on the topographic surfaces illustrate the locations of the sources and receivers used in the inversions.

102x148mm (300 x 300 DPI)

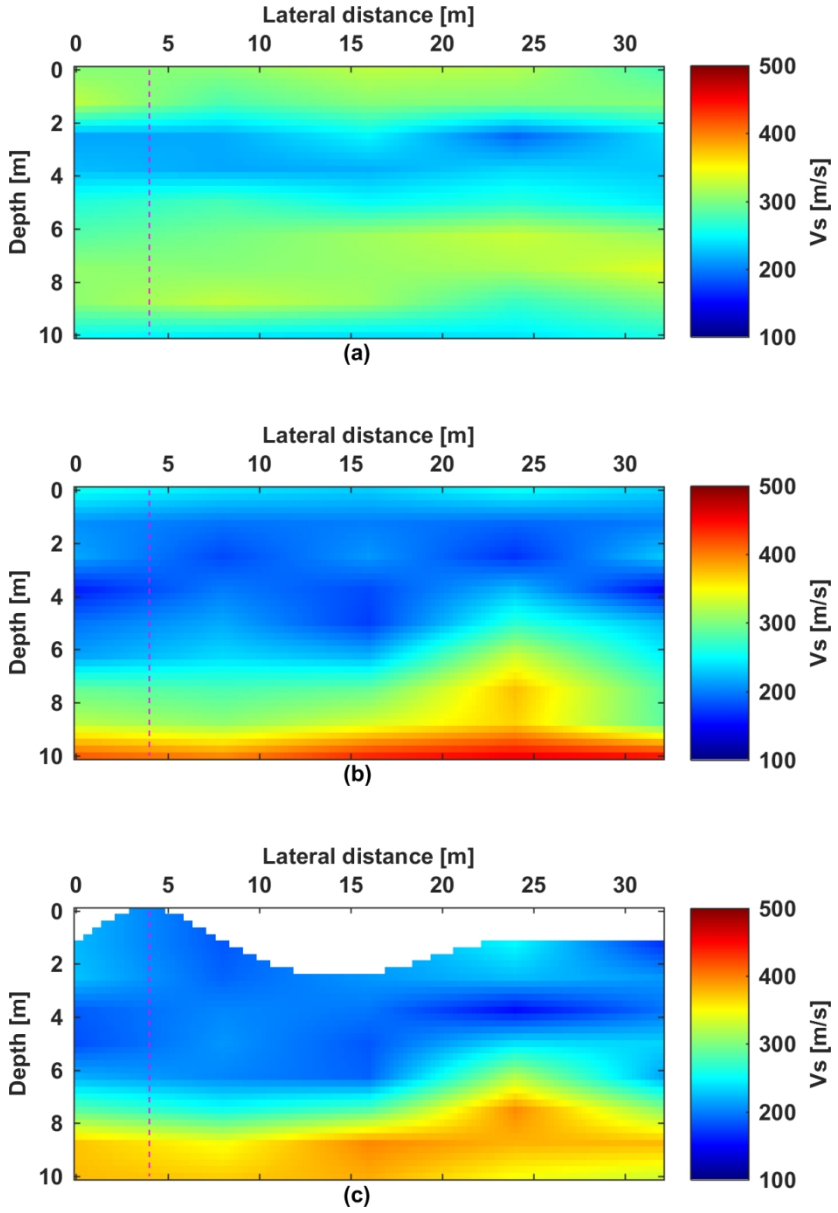

Figure 4. The predicted Vs models corresponding to the best seismograms (minimum data misfits): (a) 1D model; (b) 2D model; (c) 2D irregular-topography model. The dashed magenta lines indicate the positions of the 1D Vs profiles that will be presented in Figure 5. Note that the long-wavelength structures of the reference models (Figure 3) have been fairly reproduced.

102x148mm (300 x 300 DPI)

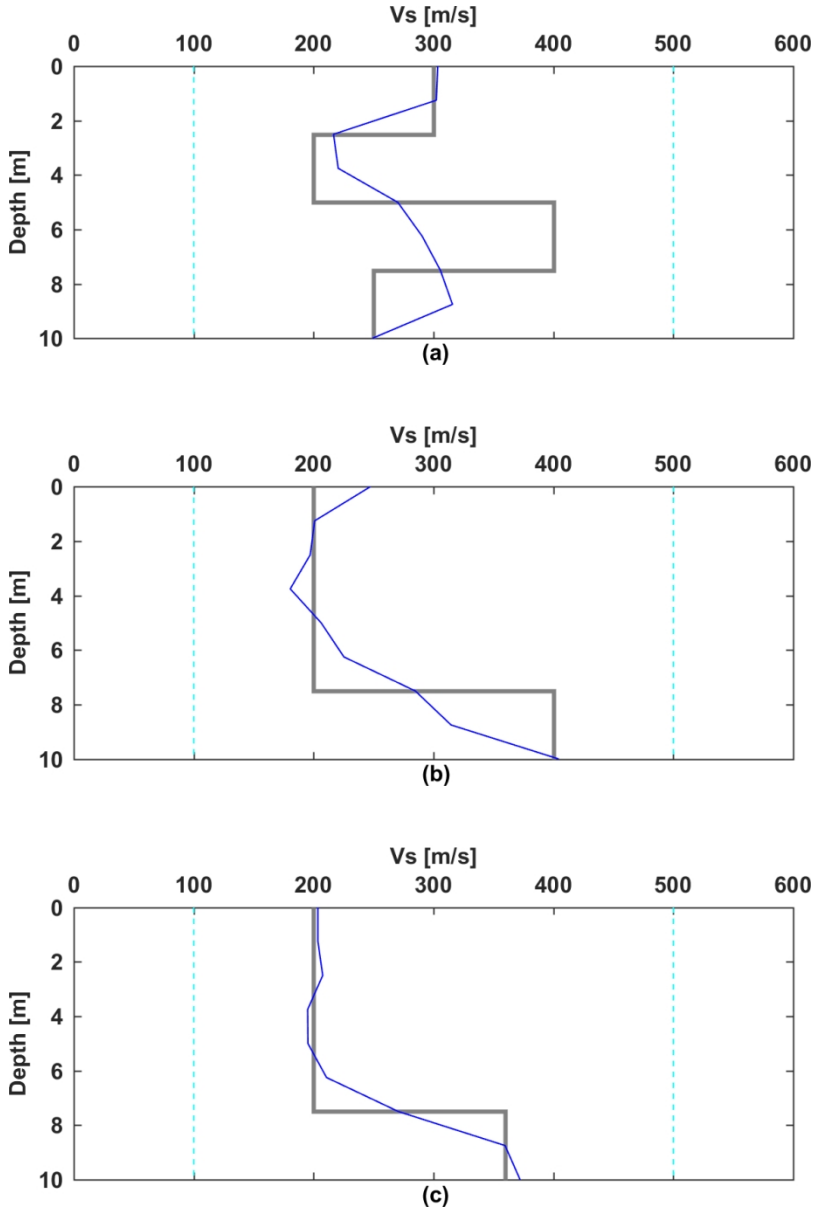

Figure 5. The Vs profiles picked from the reference (Figure 3) and predicted (Figure 4) models at the lateral distance of 4 m. From (a) to (c) the profiles sequentially correspond with the 1D model, the 2D model and the 2D irregular-topography model. The profiles picked from the reference models are drawn in gray while those picked from the predicted models are presented in blue. The dashed cyan lines show the Vs search ranges in our genetic-algorithm FWI. Note that the search ranges are wide and constant, that is, they do not follow the trends of the reference Vs profiles, and that the predicted Vs profiles fairly match the reference model profiles.

99x148mm (300 x 300 DPI)

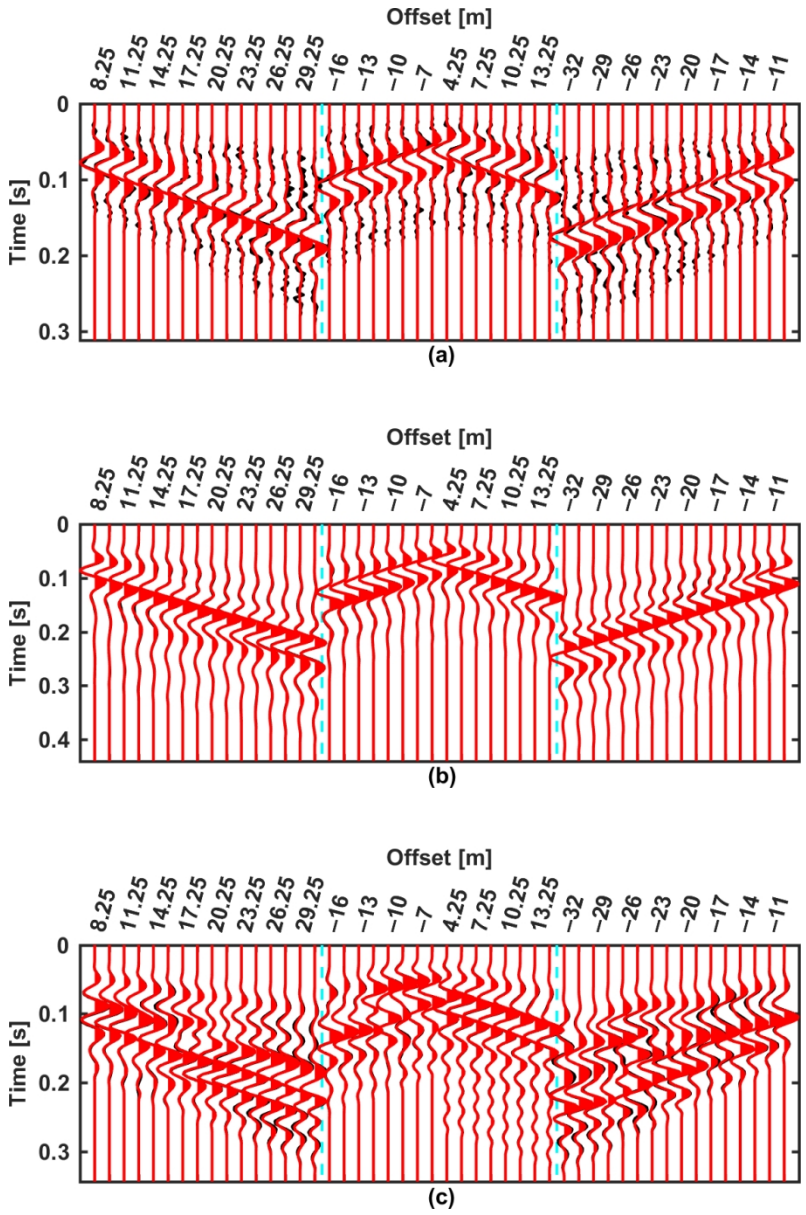

Figure 6. The "observed" (black traces) and predicted (red traces) best seismograms related to the (a) 1D model, (b) 2D model and (c) 2D irregular-topography model. One every six traces is plotted. The observed seismograms in (a) have been contaminated with weak random noise. The dashed cyan lines delimit the left, middle and right shot gathers. The seismograms have been normalized trace by trace. The matching between observed and predicted seismograms is quite good at all offsets.

98x148mm (300 x 300 DPI)

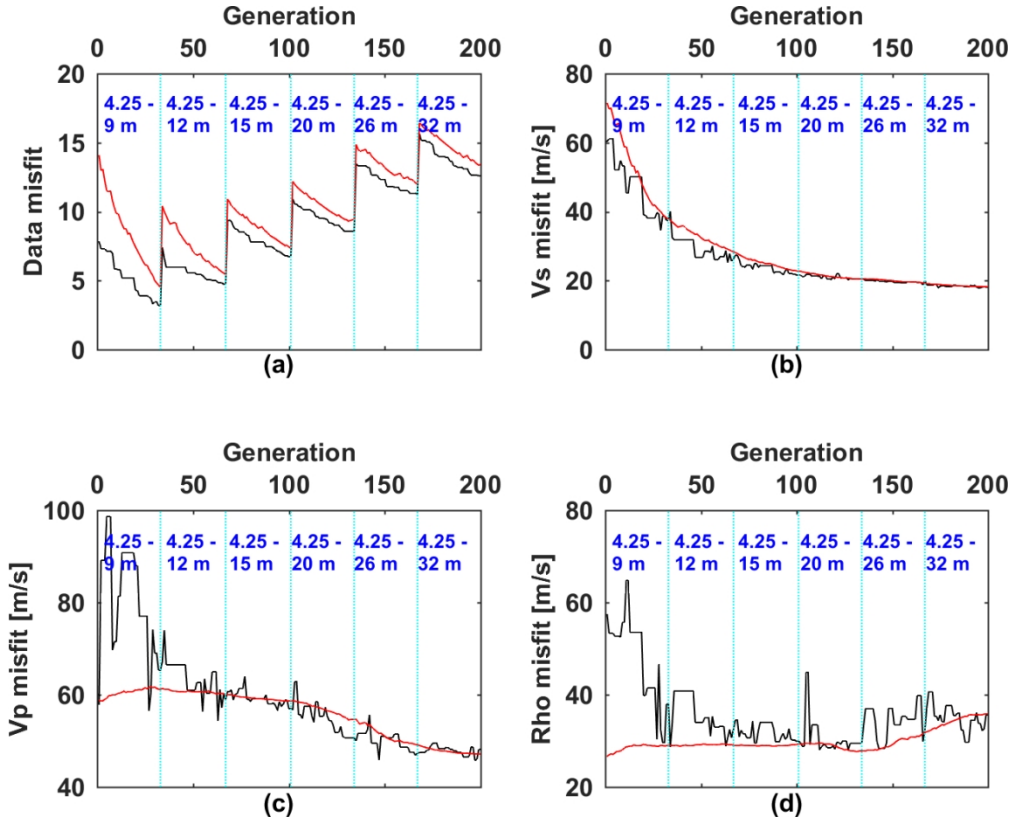

Figure 7. The evolution of the data and model misfits for the 3rd example: (a) data misfits; (b) Vs-model misfits; (c) Vp-model misfits; (d) Rho-model misfits. The black and red curves in (a) indicate the minimum data misfits and the mean data misfits, respectively. In (b), (c) and (d) the black curve shows the misfits of the Vs, Vp and Rho models associated with the seismograms giving the minimum data misfits (best seismograms), while the red curve represents the misfits of the mean models calculated over the entire population. The blue annotations delimited by the dashed cyan lines indicate the offset ranges of the data inverted at each phase of the offset-marching frame.

110x89mm (300 x 300 DPI)

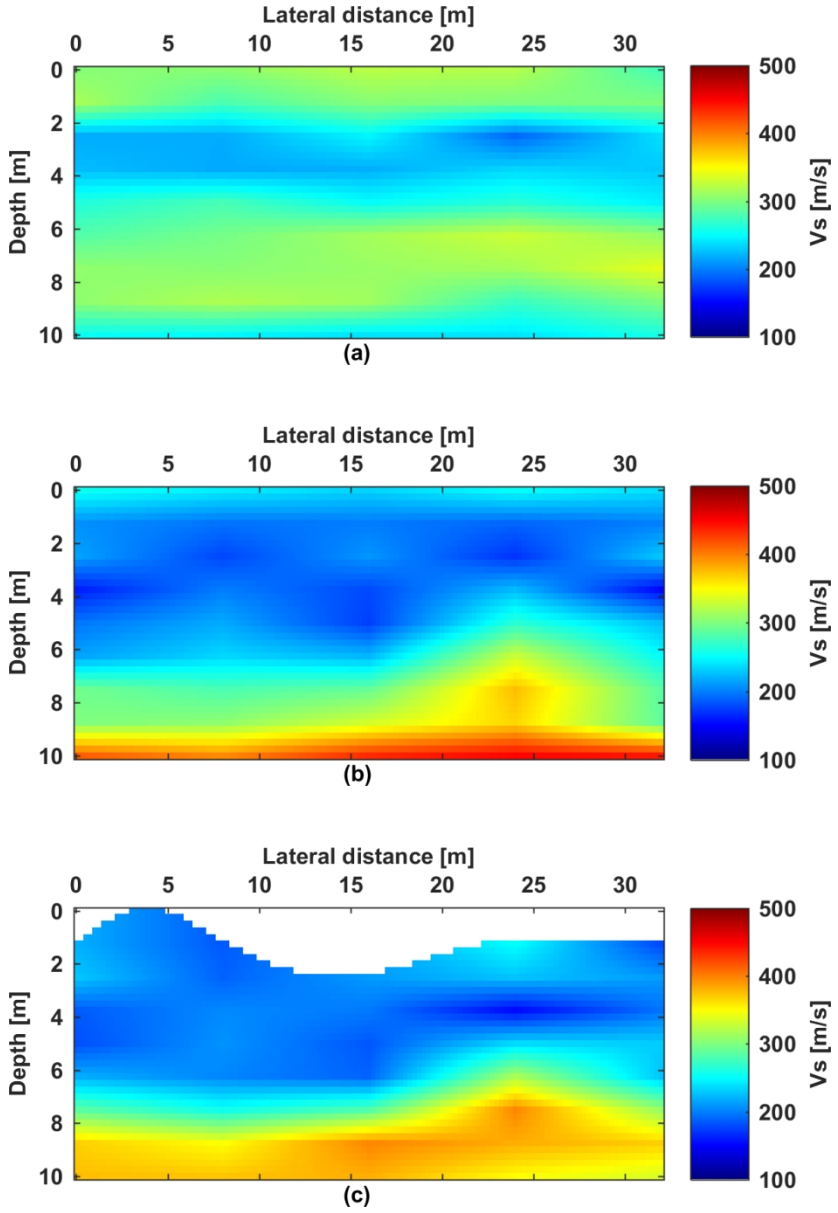

Figure 8. The mean of the Vs models at the last generations of our genetic-algorithm Rayleigh-wave FWI: (a) 1D model; (b) 2D model; (c) 2D irregular-topography model. These mean models are rather similar to the best models presented in Figure 4.

102x148mm (300 x 300 DPI)

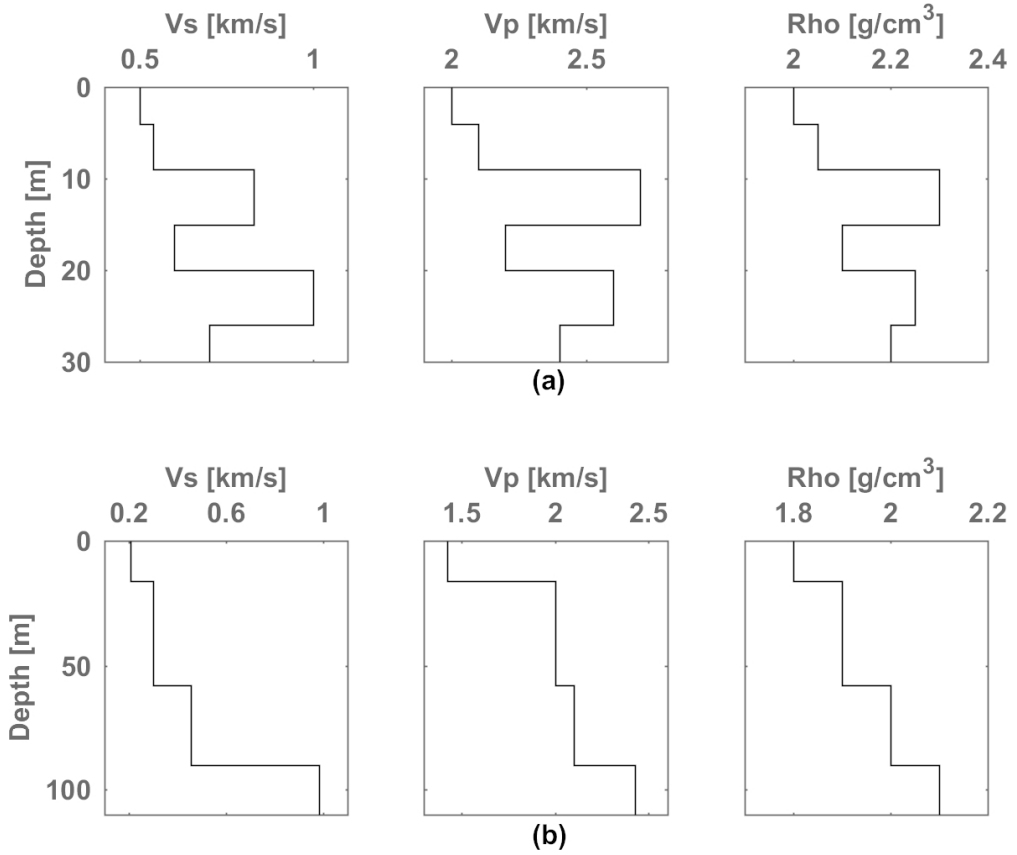

Figure B-1. Models used for checking the effectivity of the adopted 3D to 2D correction (Forbriger et al., 2014) method. (a) A synthetic model that contains sharp velocity contrasts and velocity inversions. (b) A realistic model derived from three-component down-hole recordings and density log.

100x85mm (300 x 300 DPI)

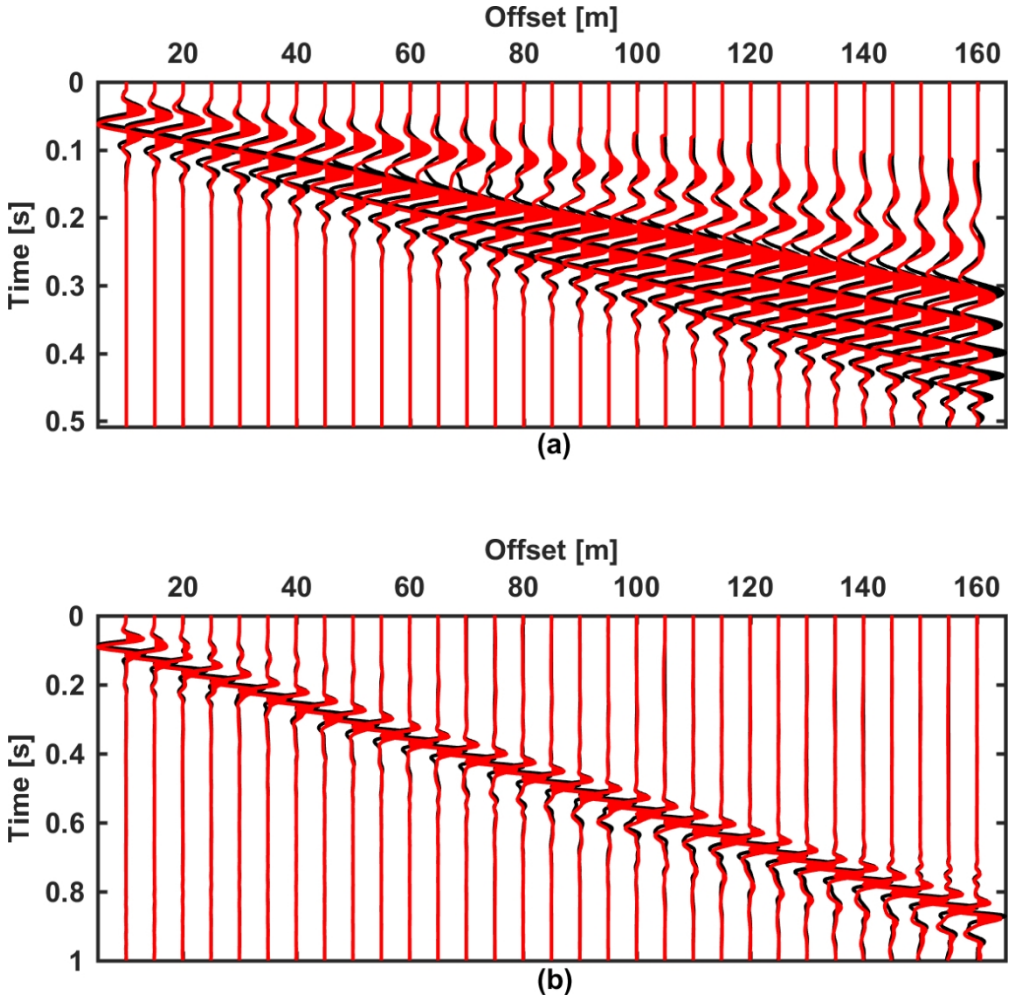

Figure B-2. Reflectivity modeling results of (a) the model in Figure B-1a and (b) the model in Figure B-1b. The black and red seismograms are the reflectivity modeling outcomes before and after the application of the 3D to 2D correction, respectively. The seismograms have been normalized trace by trace. The phase differences are evident at the whole offset range.

98x97mm (300 x 300 DPI)

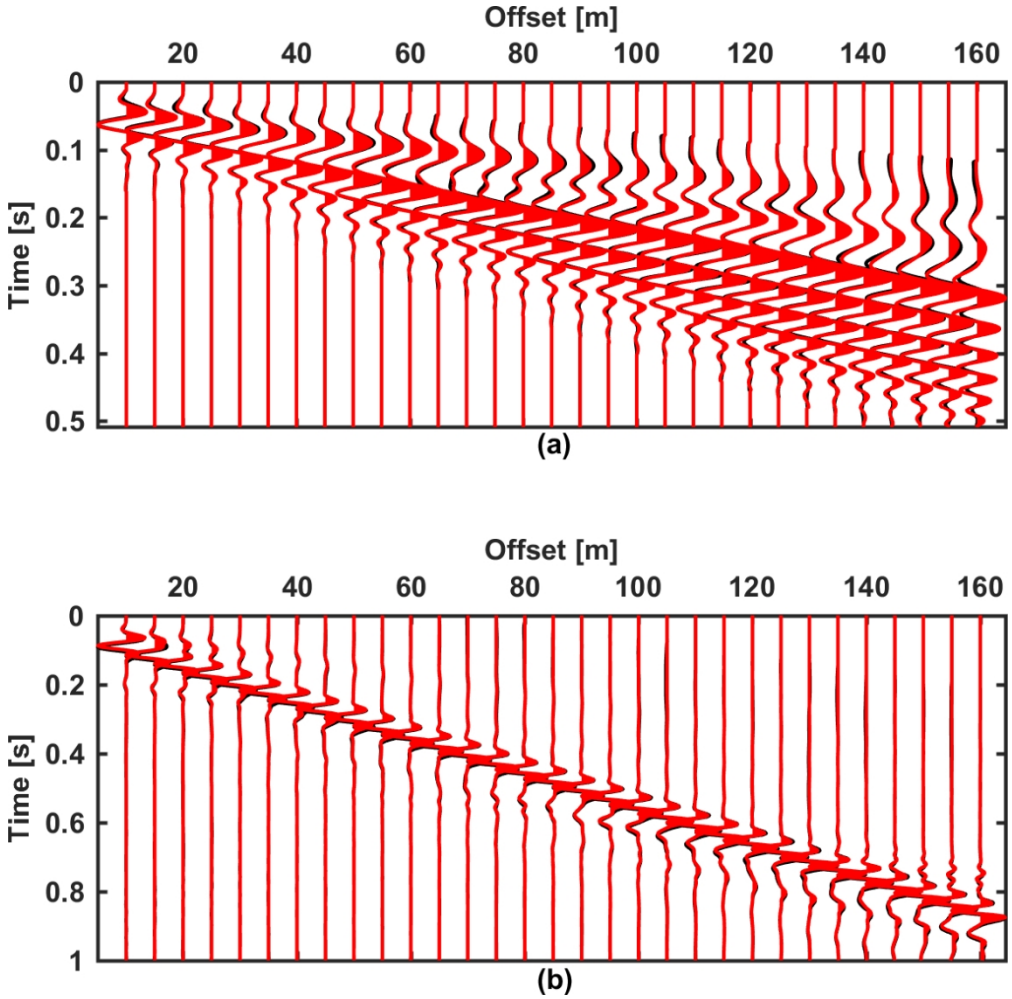

Figure B-3. Modeling outcomes of (a) the model in Figure B-1a and (b) the model in Figure B-1b. The black seismograms are the results of reflectivity modeling with the 3D to 2D correction applied, while the red seismograms are outcomes of the employed 2D FDM code. The seismograms have been normalized trace by trace. In both (a) and (b), the black and red seismogram satisfactorily match, even at the farthest offset.

98x97mm (300 x 300 DPI)

DATA AND MATERIALS AVAILABILITY

Data associated with this research are available and can be obtained by contacting the corresponding author.